Wall thickness effect on the resistive wall mode stability in toroidal plasmas

L.-J. Zheng and M. T. Kotschenreuther
Institute for Fusion Studies, University of Texas at Austin, Austin, Texas 78712

(Received 8 March 2005; accepted 6 May 2005; published online 20 June 2005)

The effect of finite wall thickness on the stability of $n=1$ resistive wall modes in toroidal plasmas is investigated. A fusion reactor-relevant configuration is examined. The investigation employs a novel ideal-magnetohydrodynamics adaptive shooting code for axisymmetric plasmas, extended to take into account the wall thickness. Although finite wall thickness generally reduces the growth rate of the resistive wall modes, no contribution to stabilization is found to be made by the portion of the wall that is located beyond the critical position for perfectly conducting wall stabilization. Thus, when the inner side of the wall lies near the critical wall position, the scaling of the growth rate versus wall thickness in the realistic thick-wall calculation is significantly different from that of the usual thin-wall theory. The thin-wall estimate is relevant only when the wall is brought very close to the plasma and is not too thick. © *2005 American Institute of Physics*. [DOI: 10.1063/1.1943347]

I. INTRODUCTION

The stability of large-scale magnetohydrodynamic (MHD) modes is vital to the magnetic confinement of toroidal plasmas, such as the International Thermonuclear Experimental Reactor (ITER).[1] In tokamaks, the maximum achievable value of the parameter β (viz., the ratio of the plasma pressure to the magnetic field pressure) is limited by pressure-driven external kink modes. The numerical work by Troyon *et al.*[2] found that the maximum achievable value of the no-wall beta limit $\beta_{\max}$ is proportional to the plasma current I_p. In order to reflect this scaling, the normalized beta parameter $\beta_N=\beta_{\max}a(m)B_0(T)/I_p(MA)$ was introduced, where a is the minor radius and B_0 is the magnetic field strength at the magnetic axis. Early computations[2] gave $\beta_N \approx 2.8$. Later, after further optimization of the pressure and current profiles and the geometric parameters (such as the triangularity, elongation, and squareness), it was shown that $\beta_N \approx 4$ could be attained.[3–6]

These computed values for the β limit did not take into account the stabilization due to a conducting wall. Furthermore, all real conducting walls possess non-negligible resistivity. Hence, modes that are stabilized by a perfectly conducting wall can be converted into unstable resistive wall modes. A theory based on the thin-wall approximation showed that the resistive wall mode growth rate is inversely proportional to the magnetic diffusion time of the resistive wall, $\tau_w=\mu_0\sigma\bar{b}d$, where μ_0 is the vacuum permeability, σ denotes the wall conductivity, $\bar{b}$ represents the average wall radius, and d is the thickness of the wall.[7] In this thin-wall estimate, the growth rate was found to be inversely proportional to the thickness of the wall. This scaling predicts that an increase in the wall thickness could result in reduction of the resistive wall mode growth rate.

However, we note that the actual wall of a fusion reactor will not be thin. For example, the steel neutron shield in the design for ITER will be about 0.45 m thick. Reactor blankets with liquid-metal breeder materials would be even thicker. Therefore, investigation of the effect of finite wall thickness is a subject of practical interest. In particular, we expect that thick walls will have an effect on the stability of the resistive wall mode. Other mechanisms for the resistive wall mode stabilization are plasma rotation[8–13] and active feedback.[14] In the present work we limit our consideration to the effect of thick walls on the growth rate of the resistive wall mode.

Our investigation employs the newly developed ideal-MHD shooting code AEGIS (adaptive eigenfunction independent solutions).[15] The AEGIS code uses an adaptive-mesh shooting method in the radial direction and therefore has a good resolution near mode resonance surfaces. By extending its wall package in the current work, we were able to apply the AEGIS code in order to address the effect of wall thickness on the resistive wall mode stability. A configuration like that of ITER (Ref. 1) was examined. We found that the scaling of the growth rate versus wall thickness in the realistic thick-wall calculation is significantly different from that of the usual thin-wall theory. No contribution to stabilization is contributed by the portion of the wall that is located beyond the critical position for perfectly conducting wall stabilization.

The paper is structured as follows: In the following section, the theoretical formulation for a resistive thick wall is described. In Sec. III, the numerical results are presented. In the last section, we offer conclusions and discussion.

II. THEORETICAL FORMULATION

In this section, we describe the numerical scheme for studying the effect of wall thickness on the stability of the resistive wall modes. The plasma-wall system consists of four parts: the plasma torus, the vacuum region between the plasma and the wall (the inner vacuum region), the thick wall, and the vacuum region outside the wall (the outer vacuum region). The radial locations of the interfaces between the plasma and the inner vacuum region, between the inner vacuum region and the wall, and between the wall and the outer vacuum region are represented by ψ_a, ψ_{b_1}, and ψ_{b_2},

respectively, where ψ_a is the poloidal magnetic flux inside the plasma, and ψ_{b_1} and ψ_{b_2} are the radial coordinates for the inner and outer edges of the wall. The theory for the plasma region has been described in Ref. 15. The theory for the inner vacuum region is also similar to that outlined in Ref. 15. The theory for the outer vacuum region is given in Ref. 16. Therefore, our effort in the present work is focused on the description for the thick-wall region and on the process for matching from one region to the next.

A. Theoretical formulation for the plasma region

Since the detailed formalism for the plasma region is already described in Ref. 15, here we merely review the main points. The total plasma energy δW_p consists of the potential energy and the kinetic energy. Magnetic flux coordinates (ψ, θ, ϕ) are introduced to simplify the energy, where ψ is the magnetic flux inside the reference surface, θ is the poloidal angle, and ϕ is the toroidal axisymmetric angle. Due to the toroidal axisymmetry, only a single Fourier component in ϕ is needed, with toroidal mode number n. Fourier decomposition is performed in terms of the poloidal angle θ, with the total number of Fourier components taken into account being denoted as M. After minimization with respect to the compressional Alfvén mode, the plasma energy can be reduced to[15]

$$\delta W_p = \frac{1}{2\mu_0}\int d\psi[\boldsymbol{\xi}_\psi'^{\dagger}(\mathcal{F}\boldsymbol{\xi}_\psi' + \mathcal{K}\boldsymbol{\xi}_\psi) + \boldsymbol{\xi}_\psi^{\dagger}(\mathcal{K}^{\dagger}\boldsymbol{\xi}_\psi' + \mathcal{G}\boldsymbol{\xi}_\psi)], \tag{1}$$

where $\mathcal{F}$, $\mathcal{K}$, and $\mathcal{G}$ are $M\times M$ equilibrium matrices (whose detailed definitions are given in the Appendix), $\boldsymbol{\xi}_\psi$ is a vector in Fourier space (i.e., an $M\times 1$ matrix) whose elements are the poloidal Fourier components of the radial magnetic field line displacement, and the prime denotes a derivative with respect to ψ.

The set of Euler-Lagrange equations for Eq. (1) is

$$\mathbf{u}_p' = \mathcal{L}_p\mathbf{u}_p, \tag{2}$$

where

$$\mathbf{u}_p \equiv \begin{pmatrix}\mathbf{u}_{p1}\\ \mathbf{u}_{p2}\end{pmatrix} = \begin{pmatrix}\boldsymbol{\xi}^{\psi}\\ \mathcal{F}\boldsymbol{\xi}^{\psi\prime} + \mathcal{K}\boldsymbol{\xi}^{\psi}\end{pmatrix},$$

$$\mathcal{L}_p = \begin{pmatrix}-\mathcal{F}^{-1}\mathcal{K} & \mathcal{F}^{-1}\\ \mathcal{G}-\mathcal{K}^{\dagger}\mathcal{F}^{-1}\mathcal{K} & \mathcal{K}^{\dagger}\mathcal{F}^{-1}\end{pmatrix}.$$

Equation (2) constitutes a set of $2M$ equations. With M boundary conditions imposed at the magnetic axis, there are M independent solutions, which are denoted as

$$\mathbf{u}_p^k \equiv \begin{pmatrix}\mathbf{u}_{p1}^k\\ \mathbf{u}_{p2}^k\end{pmatrix}, \quad k = 1,\ldots,M.$$

These independent solutions can be obtained by the method of numerical shooting from the magnetic axis to the plasma edge. A linear combination of the M independent solutions can be used to represent the general solution of Eq. (2),

$$\mathbf{u}_p = \mathcal{U}_p\mathbf{c}_p, \tag{3}$$

where the independent solution matrix is given as follows:

$$\mathcal{U}_p \equiv \begin{pmatrix}\mathcal{U}_{p1}\\ \mathcal{U}_{p2}\end{pmatrix} = \begin{pmatrix}\mathbf{u}_{p1}^1\cdots\mathbf{u}_{p1}^M\\ \mathbf{u}_{p2}^1\cdots\mathbf{u}_{p2}^M\end{pmatrix}.$$

Here, $\mathbf{c}_p$ is a constant vector (i.e., an $M\times 1$ matrix), which can be determined by the boundary conditions at the plasma-vacuum interface.

Using the general solution expressed in Eq. (3), we minimize the plasma energy as

$$\delta W_p = \frac{1}{2\mu_0}[\mathbf{c}_p^{\dagger}\mathcal{U}_{p1}^{\dagger}\mathcal{U}_{p2}\mathbf{c}_p]^{\psi=\psi_a}. \tag{4}$$

B. Theoretical formulation for the inner vacuum region

Introducing φ to denote the scalar potential, we can express the energy for the inner vacuum region as

$$\delta W_v = \frac{1}{2\mu_0}\int dV|\nabla\varphi|^2, \tag{5}$$

where dV represents the volume element. In this vacuum region, we construct the coordinate system (ψ, θ, ϕ), where ψ and θ represent the radial and poloidal coordinates (for example, based on equal distance grids). Fourier decomposition is performed with respect to the poloidal coordinate θ. The expression for the energy in Eq. (5) is reduced to

$$\delta W_v = \frac{1}{2\mu_0}\int d\psi[\boldsymbol{\varphi}'^{\dagger}(\mathcal{F}_v\boldsymbol{\varphi}' + \mathcal{K}_v\boldsymbol{\varphi}) + \boldsymbol{\varphi}^{\dagger}(\mathcal{K}^{\dagger}{}_v\boldsymbol{\varphi}' + \mathcal{G}_v\boldsymbol{\varphi})], \tag{6}$$

where $\mathcal{F}_v = \langle\mathcal{J}|\nabla\psi|^2\rangle$, $\mathcal{K}_v = i\langle\mathcal{J}\boldsymbol{\nabla}\psi\cdot\boldsymbol{\nabla}\theta\rangle\mathcal{M}$, and $\mathcal{G}_v = \mathcal{M}\langle\mathcal{J}|\nabla\theta|^2\rangle\mathcal{M} + n^2\langle\mathcal{J}/X^2\rangle$. The definitions for $\mathcal{J}$, $\mathcal{M}$, and X are given in the Appendix and $\boldsymbol{\varphi}$ is a vector in Fourier space, whose elements are the poloidal Fourier components of the potential φ.

As in the plasma region, an Euler-Lagrange equation is used to minimize the vacuum energy. Instead of using the Green function method, we employ the shooting method to solve the Euler-Lagrange equations, which are given as follows:

$$\mathbf{u}_v' = \mathcal{L}_v\mathbf{u}_v, \tag{7}$$

where

$$\mathbf{u}_v \equiv \begin{pmatrix}\mathbf{u}_{v1}\\ \mathbf{u}_{v2}\end{pmatrix} = \begin{pmatrix}\boldsymbol{\varphi}\\ \mathcal{F}_v\boldsymbol{\varphi}' + \mathcal{K}_v\boldsymbol{\varphi}\end{pmatrix},$$

$$\mathcal{L}_v = \begin{pmatrix}-\mathcal{F}_v^{-1}\mathcal{K}_v & \mathcal{F}_v^{-1}\\ \mathcal{G}_v-\mathcal{K}_v^{\dagger}\mathcal{F}_v^{-1}\mathcal{K}_v & \mathcal{K}_v^{\dagger}\mathcal{F}_v^{-1}\end{pmatrix}.$$

Equation (7) constitutes a set of $2M$ equations and therefore has two sets of M independent solutions:

$$u_v^{\mathrm{I}k} \equiv \begin{pmatrix} \mathbf{u}_{v1}^{\mathrm{I}k} \\ \mathbf{u}_{v2}^{\mathrm{I}k} \end{pmatrix}, \quad u_v^{\mathrm{II}k} \equiv \begin{pmatrix} \mathbf{u}_{v1}^{\mathrm{II}k} \\ \mathbf{u}_{v2}^{\mathrm{II}k} \end{pmatrix}, \quad k = 1, \cdots, M.$$

The independent solutions can be obtained by the procedure of numerical shooting from ψ_{b_1} to ψ_a, with the following boundary conditions imposed at ψ_{b_1}:

$$\mathcal{U}_v^{\mathrm{I}} \equiv \begin{pmatrix} \mathcal{U}_{v1}^{\mathrm{I}} \\ \mathcal{U}_{v2}^{\mathrm{I}} \end{pmatrix} \equiv \begin{pmatrix} \mathbf{u}_{v1}^{\mathrm{I}1} \cdots \mathbf{u}_{v1}^{\mathrm{I}M} \\ \mathbf{u}_{v2}^{\mathrm{I}1} \cdots \mathbf{u}_{v2}^{\mathrm{I}M} \end{pmatrix} = \begin{pmatrix} \mathcal{I} \\ \mathcal{O} \end{pmatrix},$$

$$\mathcal{U}_v^{\mathrm{II}} \equiv \begin{pmatrix} \mathcal{U}_{v1}^{\mathrm{II}} \\ \mathcal{U}_{v2}^{\mathrm{I}} \end{pmatrix} \equiv \begin{pmatrix} \mathbf{u}_{v1}^{\mathrm{II}1} \cdots \mathbf{u}_{v1}^{\mathrm{II}M} \\ \mathbf{u}_{v2}^{\mathrm{II}1} \cdots \mathbf{u}_{v2}^{\mathrm{II}M} \end{pmatrix} = \begin{pmatrix} \mathcal{O} \\ \mathcal{I} \end{pmatrix}.$$

Here $\mathcal{I}$ is the unity matrix of rank $M \times M$, and $\mathcal{O}$ is the zero matrix of rank $M \times M$. The general solution can then be constructed as a linear combination of the independent solutions:

$$\mathbf{u}_v = \mathcal{U}_v^{\mathrm{I}} \mathbf{c}_v^{\mathrm{I}} + \mathcal{U}_v^{\mathrm{II}} \mathbf{c}_v^{\mathrm{II}}, \tag{8}$$

where $\mathbf{c}_v^{\mathrm{I,II}}$ are constant vectors of rank $M \times 1$ to be determined by the boundary matching conditions.

Using the solution of Eq. (8), we reduce the expression for the energy in Eq. (6) to

$$\delta W_{v_1} = \frac{1}{2\mu_0} [(\mathbf{c}_v^{\mathrm{I}\dagger} \mathcal{U}_{v1}^{\mathrm{I}\dagger} + \mathbf{c}_v^{\mathrm{II}\dagger} \mathcal{U}_{v1}^{\mathrm{II}\dagger})(\mathcal{U}_{v2}^{\mathrm{I}} \mathbf{c}_v^{\mathrm{I}} + \mathcal{U}_{v2}^{\mathrm{II}} \mathbf{c}_v^{\mathrm{II}})]_{\psi=\psi_a}^{\psi=\psi_{b_1}}. \tag{9}$$

C. Theoretical formulation for the outer vacuum region

The formalism for the vacuum region outside the wall has been described in Ref. 16. The energy in this region can be expressed as

$$\delta W_{v_2} = \frac{1}{2\mu_0} \int dV |\nabla \varphi|^2.$$

The corresponding Euler-Lagrange equation is just the Laplace equation

$$\nabla^2 \varphi = 0.$$

This equation can be solved by Green's function method. With the boundary condition $\varphi \to 0$ at infinity, the solution at the outer boundary of the wall ψ_{b_2} can be expressed as

$$\mathbf{u}_{g1} = \mathcal{S} \mathbf{u}_{g2}, \tag{10}$$

where $\mathbf{u}_{g1}$ is a vector in Fourier space with the Fourier components of φ as its elements, $\mathbf{u}_{g2}$ is a vector with the Fourier components of $\mathcal{J} \nabla \psi \cdot \nabla \varphi$ as its elements, and the $M \times M$ matrix $\mathcal{S} = \mathcal{S}_l^{-1} \mathcal{S}_r$ is constructed from

$$\mathcal{S}_{lmm'} = \delta_{mm'} - \frac{1}{\pi} P \int_0^{\pi} d\theta \int_{\theta-\pi}^{\theta+\pi} \cos(m'\theta' - m\theta) \times \mathcal{K}^n(\theta, \theta') d\theta',$$

$$\mathcal{S}_{rmm'} = -\frac{1}{\pi} \int_0^{\pi} d\theta \int_{\theta-\pi}^{\theta+\pi} \cos(m'\theta' - m\theta) \mathcal{G}^n(\theta, \theta') d\theta'.$$

Here, $\mathcal{G}^n(\theta, \theta')$ and $\mathcal{K}^n(\theta, \theta')$ are two-dimensional Green functions, as defined in Ref. 16, and $P\int$ denotes principal-part integration.

Using the solution [Eq. (10)] of the Euler-Lagrange equation, the energy in the outer vacuum region can be expressed as

$$\delta W_{v_2} = \frac{1}{2\mu_0} [\mathbf{u}_{g1}^{\dagger} \mathbf{u}_{g2}]_{\psi=\psi_{b_2}}. \tag{11}$$

D. Theoretical formulation for the thick wall

First, we construct a coordinate system (ψ, θ, ϕ) in the wall region, with ψ representing the radial coordinate and θ being the poloidal angle (for example, based on equal distance grids). In this coordinate system the components of the metric transformation can be expressed as follows:

$$g_{11} = \mathcal{J}^2 \nabla \theta \times \nabla \phi \cdot \nabla \theta \times \nabla \phi,$$

$$g_{22} = \mathcal{J}^2 \nabla \phi \times \nabla \psi \cdot \nabla \phi \times \nabla \psi,$$

$$g_{33} = \mathcal{J}^2 \nabla \psi \times \nabla \theta \cdot \nabla \psi \times \nabla \theta,$$

$$g_{12} = \mathcal{J}^2 \nabla \theta \times \nabla \phi \cdot \nabla \phi \times \nabla \psi,$$

$$g_{23} = g_{31} = 0.$$

Configuration space vectors—for example, $\delta \mathbf{B}$—can be decomposed into their covariant and contravariant components in this coordinate system as follows:

$$\delta \mathbf{B} = \delta B_{\psi} \nabla \psi + \delta B_{\theta} \nabla \theta + \delta B_{\phi} \nabla \phi,$$

$$\delta \mathbf{B} = \delta B^{\psi} \mathcal{J} \nabla \theta \times \nabla \phi + \delta B^{\theta} \mathcal{J} \nabla \phi \times \nabla \psi + \delta B^{\phi} \mathcal{J} \nabla \psi \times \nabla \theta.$$

We introduce the vector potential $\delta \mathbf{A}$, such that

$$\delta \mathbf{B} = \nabla \times \delta \mathbf{A}, \tag{12}$$

$$\delta \mathbf{E} = -\lambda \delta \mathbf{A}.$$

Here, the electrostatic potential gauge $\varphi = 0$ has been employed;[17] $\delta \mathbf{E}$ represents the perturbed electric field, and λ is the growth rate of the mode.

The energy in the wall region can be expressed as[17]

$$\delta W_w = \frac{1}{2\mu_0} \int dV (|\nabla \times \delta \mathbf{A}|^2 + \mu_0 \sigma \lambda |\delta \mathbf{A}|^2). \tag{13}$$

The corresponding Euler-Lagrange equation is simply given by

$$\nabla \times \delta\mathbf{B} = -\mu_0 \sigma\lambda\, \delta\mathbf{A}. \tag{14}$$

For the solution of the Euler-Lagrange equation, the energy in Eq. (13) is minimized to

$$\delta W_w = \frac{1}{2\mu_0}[\delta\boldsymbol{\mathcal{A}}_\theta^\dagger \delta\boldsymbol{\mathcal{B}}_\phi - \delta\boldsymbol{\mathcal{A}}_\phi^\dagger \delta\boldsymbol{\mathcal{B}}_\theta]_{\psi=\psi_{b_1}}^{\psi=\psi_{b_2}}. \tag{15}$$

Here $\boldsymbol{\mathcal{A}}_{\theta,\phi}$ and $\boldsymbol{\mathcal{B}}_{\theta,\phi}$ are vectors in Fourier space with the Fourier components of the corresponding quantities as their elements.

The basic set of equations (12) and (14) can be used to determine $\delta\mathbf{A}$ completely. Note that only four out of the six equations are actually independent. This leads us to define the following four independent variables:

$$y_1 = \mathcal{J}\delta B^\psi, \quad y_2 = i\delta B_\theta, \quad y_3 = i\delta B_\phi, \quad y_4 = i\mu_0\sigma\lambda\frac{1}{n}\delta A_\phi. \tag{16}$$

Boldface $\mathbf{y}_i$ is used to denote the respective vectors in Fourier space. After performing the poloidal Fourier decomposition, we can reduce the basic set of equations (12) and (14) to

$$\begin{pmatrix} \mathbf{y}_1' \\ \mathbf{y}_2' \\ \mathbf{y}_3' \\ \mathbf{y}_4' \end{pmatrix} = \begin{pmatrix} \mathcal{D}_{11} & \mathcal{D}_{12} & \mathcal{D}_{13} & 0 \\ \mathcal{D}_{21} & \mathcal{D}_{11} & 0 & -\mathcal{D}_{13} \\ \mathcal{D}_{31} & 0 & -\tilde{\mathcal{D}}_{11} & \tilde{\mathcal{D}}_{12} \\ 0 & -\mathcal{D}_{31} & \tilde{\mathcal{D}}_{21} & -\tilde{\mathcal{D}}_{11} \end{pmatrix} \begin{pmatrix} \mathbf{y}_1 \\ \mathbf{y}_2 \\ \mathbf{y}_3 \\ \mathbf{y}_4 \end{pmatrix}, \tag{17}$$

where tilde represents matrix transpose, and

$$\mathcal{D}_{11} = \mathcal{M} i \left\langle \frac{g_{12}}{g_{22}} \right\rangle,$$

$$\mathcal{D}_{12} = -\mathcal{M} \left\langle \frac{\mathcal{J}}{g_{22}} \right\rangle,$$

$$\mathcal{D}_{13} = n \left\langle \frac{\mathcal{J}}{g_{33}} \right\rangle,$$

$$\mathcal{D}_{21} = \mathcal{M} \left\langle \frac{1}{\mathcal{J}} \left(g_{11} - \frac{g_{12}^2}{g_{22}} \right) \right\rangle,$$

$$\mathcal{D}_{31} = \left\langle \mu_0\sigma\lambda \frac{\mathcal{J}}{n g_{22}} + n \frac{1}{\mathcal{J}} \left(g_{11} - \frac{g_{12}^2}{g_{22}} \right) \right\rangle.$$

The definition of $\langle \cdots \rangle$ is given in the Appendix. The first row of Eq. (17) results from $\nabla \cdot \delta\mathbf{B} = 0$. The second row is the $\nabla\phi$ projection of Eq. (14). The third row is derived from the $\nabla\theta$ projection of Eq. (14). The last equation is obtained by the use of the $\nabla\theta$ projection of Eq. (12) and the $\nabla\psi$ projection of Eq. (14).

The wall meets the vacuum regions on both sides. The three components of $\delta\mathbf{B}$ are required to be continuous across the two wall-vacuum interfaces. Equations (17) can be solved by the procedure of numerical shooting from ψ_{b_2} to ψ_{b_1}, with the boundary conditions at ψ_{b_2} imposed as the initial shooting conditions. Two sets of initial conditions can be chosen as follows:

$$\begin{pmatrix} \mathcal{Y}_1^{\mathrm{I}} \\ \mathcal{Y}_2^{\mathrm{I}} \\ \mathcal{Y}_3^{\mathrm{I}} \\ \mathcal{Y}_4^{\mathrm{I}} \end{pmatrix}^{\psi=\psi_{b_2}} \equiv \begin{pmatrix} \mathbf{y}_1^{\mathrm{I}1} \cdots \mathbf{y}_1^{\mathrm{I}M} \\ \mathbf{y}_2^{\mathrm{I}1} \cdots \mathbf{y}_2^{\mathrm{I}M} \\ \mathbf{y}_3^{\mathrm{I}1} \cdots \mathbf{y}_3^{\mathrm{I}M} \\ \mathbf{y}_4^{\mathrm{I}1} \cdots \mathbf{y}_4^{\mathrm{I}M} \end{pmatrix}^{\psi=\psi_{b_2}} = \begin{pmatrix} \mathcal{I} \\ \mathcal{M}\mathcal{S} \\ n\mathcal{S} \\ \mathcal{O} \end{pmatrix},$$

$$\begin{pmatrix} \mathcal{Y}_1^{\mathrm{II}} \\ \mathcal{Y}_2^{\mathrm{II}} \\ \mathcal{Y}_3^{\mathrm{II}} \\ \mathcal{Y}_4^{\mathrm{II}} \end{pmatrix}^{\psi=\psi_{b_2}} \equiv \begin{pmatrix} \mathbf{y}_1^{\mathrm{II}1} \cdots \mathbf{y}_1^{\mathrm{II}M} \\ \mathbf{y}_2^{\mathrm{II}1} \cdots \mathbf{y}_2^{\mathrm{II}M} \\ \mathbf{y}_3^{\mathrm{II}1} \cdots \mathbf{y}_3^{\mathrm{II}M} \\ \mathbf{y}_4^{\mathrm{II}1} \cdots \mathbf{y}_4^{\mathrm{II}M} \end{pmatrix}^{\psi=\psi_{b_2}} = \begin{pmatrix} \mathcal{O} \\ \mathcal{O} \\ \mathcal{O} \\ \mathcal{I} \end{pmatrix}. \tag{18}$$

Here, $\mathcal{Y}_i^{\mathrm{I,II}}$ $(i=1,\ldots,4)$ have been introduced to denote the $M \times M$ matrices consisting of the corresponding two sets of independent solutions $\mathbf{y}_{1,2}^{\mathrm{I}m}$ and $\mathbf{y}_{1,2}^{\mathrm{II}m}(m=1,\ldots,M)$. Thus, the general solutions in the wall region can be expressed as

$$\begin{pmatrix} \mathbf{y}_1 \\ \mathbf{y}_2 \\ \mathbf{y}_3 \\ \mathbf{y}_4 \end{pmatrix} = \begin{pmatrix} \mathcal{Y}_1^{\mathrm{I}} \\ \mathcal{Y}_2^{\mathrm{I}} \\ \mathcal{Y}_3^{\mathrm{I}} \\ \mathcal{Y}_4^{\mathrm{I}} \end{pmatrix} \mathbf{c}_w^{\mathrm{I}} + \begin{pmatrix} \mathcal{Y}_1^{\mathrm{II}} \\ \mathcal{Y}_2^{\mathrm{II}} \\ \mathcal{Y}_3^{\mathrm{II}} \\ \mathcal{Y}_4^{\mathrm{II}} \end{pmatrix} \mathbf{c}_w^{\mathrm{II}}.$$

Here, $\mathbf{c}_w^{\mathrm{I,II}}$ are constant vectors of rank $M \times 1$, to be determined by the matching condition at ψ_{b_1}.

Using the continuity conditions for δB_θ and δB_ϕ at ψ_{b_1}, we obtain

$$(n\mathcal{Y}_2^{\mathrm{I}} + \mathcal{M}\mathcal{Y}_3^{\mathrm{I}})\mathbf{c}_w^{\mathrm{I}} + (n\mathcal{Y}_2^{\mathrm{II}} + \mathcal{M}\mathcal{Y}_3^{\mathrm{II}})\mathbf{c}_w^{\mathrm{II}} = 0. \tag{19}$$

Therefore, we have

$$\mathbf{c}_w^{\mathrm{II}} = \mathcal{W}\mathbf{c}_w^{\mathrm{I}}, \tag{20}$$

where $\mathcal{W} = -(n\mathcal{Y}_2^{\mathrm{II}} + \mathcal{M}\mathcal{Y}_3^{\mathrm{II}})^{-1}(n\mathcal{Y}_2^{\mathrm{I}} + \mathcal{M}\mathcal{Y}_3^{\mathrm{I}})$, with quantities evaluated at ψ_{b_1}. Using the continuity conditions for δB_ψ and δB_ϕ at ψ_{b_1} and Eq. (20), we obtain

$$(\mathcal{Y}_1^{\mathrm{I}} + \mathcal{Y}_1^{\mathrm{II}}\mathcal{W})\mathbf{c}_w^{\mathrm{I}} = -\mathbf{c}_v^{\mathrm{II}}, \tag{21}$$

$$(\mathcal{Y}_3^{\mathrm{I}} + \mathcal{Y}_3^{\mathrm{II}}\mathcal{W})\mathbf{c}_w^{\mathrm{I}} = -n\mathbf{c}_v^{\mathrm{I}}. \tag{22}$$

Therefore, we obtain

$$\mathbf{c}_v^{\mathrm{II}} = \nu\mathbf{c}_v^{\mathrm{I}}, \tag{23}$$

where $\mathcal{V} = n(\mathcal{Y}_1^{\mathrm{I}} + \mathcal{Y}_1^{\mathrm{II}}\mathcal{W})(\mathcal{Y}_3^{\mathrm{I}} + \mathcal{Y}_3^{\mathrm{II}}\mathcal{W})^{-1}$, with quantities evaluated at ψ_{b_1}.

E. Eigenvalue problem

With the use of Eqs. (4), (9), (11), and (15), the total energy can be expressed as

$$\delta W = \delta W_p + \delta W_{v_1} + \delta W_w + \delta W_{v_2}$$
$$= \frac{1}{2\mu_0}[\mathbf{c}_p^\dagger \mathcal{U}_{p1}^\dagger \mathcal{U}_{p2}\mathbf{c}_p]^{\psi=\psi_a}$$
$$+ \frac{1}{2\mu_0}[(\mathbf{c}_v^{\mathrm{I}\dagger}\mathcal{U}_{v1}^{\mathrm{I}\dagger} + \mathbf{c}_v^{\mathrm{II}\dagger}\mathcal{U}_{v1}^{\mathrm{II}\dagger})(\mathcal{U}_{v2}^{\mathrm{I}}\mathbf{c}_v^{\mathrm{I}} + \mathcal{U}_{v2}^{\mathrm{II}}\mathbf{c}_v^{\mathrm{II}})]_{\psi=\psi_a}^{\psi=\psi_{b_1}}$$
$$+ \frac{1}{2\mu_0}[\delta\boldsymbol{\mathcal{A}}_\theta^\dagger \delta\boldsymbol{\mathcal{B}}_\phi - \delta\boldsymbol{\mathcal{A}}_\phi^\dagger \delta\boldsymbol{\mathcal{B}}_\theta]_{\psi=\psi_{b_1}}^{\psi=\psi_{b_2}}$$
$$+ \frac{1}{2\mu_0}[\mathbf{u}_{g1}^\dagger \mathbf{u}_{g2}]_{\psi=\psi_{b_2}}. \quad (24)$$

Note that the surface contributions in Eq. (24) represent the actual energy fluxes, i.e., the Poynting vectors. With the matching conditions at ψ_{b_2} [Eq. (18)] and at ψ_{b_1} [Eqs. (19), (21), and (22)], the opposing energy fluxes at ψ_{b_1} and ψ_{b_2} cancel each other. Only the contribution at ψ_a remains. Consequently, the total energy in Eq. (24) is reduced to

$$\delta W = \frac{1}{2\mu_0}\mathbf{c}_p^\dagger[\mathcal{U}_{p1}^\dagger \mathcal{U}_{p2}]^{\psi=\psi_a}\mathbf{c}_p$$
$$+ \frac{1}{2\mu_0}\mathbf{c}_v^{\mathrm{I}\dagger}[(\mathcal{U}_{v1}^{\mathrm{I}\dagger} + \mathcal{V}^\dagger\mathcal{U}_{v1}^{\mathrm{II}\dagger})(\mathcal{U}_{v2}^{\mathrm{I}} + \mathcal{U}_{v2}^{\mathrm{II}}\mathcal{V})]_{\psi=\psi_a}\mathbf{c}_v^{\mathrm{I}}. \quad (25)$$

Here, Eq. (23) has been used. The relationship between $\mathbf{c}_p$ and $\mathbf{c}_v^{\mathrm{I}}$ can be established from the matching condition that requires δB_ψ to be continuous at ψ_a:

$$(\mathcal{U}_{v2}^{\mathrm{I}} + \mathcal{U}_{v2}^{\mathrm{II}}\mathcal{V})\mathbf{c}_v^{\mathrm{I}} = \chi' \mathcal{K}_\parallel \mathcal{U}_{p1}\mathbf{c}_p. \quad (26)$$

Here $\mathcal{K}_\parallel$ is defined in the Appendix. With the use of Eq. (26), the total energy in Eq. (25) can be further reduced to

$$\delta W = \frac{1}{2\mu_0}\mathbf{c}_p^\dagger \mathcal{U}_{p1}^\dagger \mathcal{U}_{p2}\mathbf{c}_p - \frac{1}{2\mu_0}\mathbf{c}_p^\dagger \chi'^2 \mathcal{U}_{p1}^\dagger \mathcal{K}_\parallel (\mathcal{U}_{v2}^{\mathrm{I}}$$
$$+ \mathcal{U}_{v2}^{\mathrm{II}}\mathcal{V})^{-1\dagger}(\mathcal{U}_{v1}^{\mathrm{I}\dagger} + \mathcal{V}^\dagger\mathcal{U}_{v1}^{\mathrm{II}\dagger})\mathcal{K}_\parallel \mathcal{U}_{p1}\mathbf{c}_p, \quad (27)$$

with all quantities evaluated at the plasma edge ψ_a.

The total energy in Eq. (27) can be further minimized with respect to $\mathbf{c}_p^\dagger$. It is useful to introduce an artificial kinetic energy $\delta W_k = \Omega^2/2\mu_0 \int d\psi\, \mathbf{c}_p^\dagger \mathbf{c}_p$ in the minimization. This yields the following final eigenmode equation:

$$[\mathcal{U}_{p1}^\dagger \mathcal{U}_{p2} - \chi'^2 \mathcal{U}_{p1}^\dagger \mathcal{K}_\parallel (\mathcal{U}_{v2}^{\mathrm{I}} + \mathcal{U}_{v2}^{\mathrm{II}}\mathcal{V})^{-1\dagger}(\mathcal{U}_{v1}^{\mathrm{I}\dagger}$$
$$+ \mathcal{V}^\dagger \mathcal{U}_{v1}^{\mathrm{II}\dagger})\mathcal{K}_\parallel \mathcal{U}_{p1}]^{\psi=\psi_a}\mathbf{c}_p = \Omega^2 \mathbf{c}_p. \quad (28)$$

Note that the eigenvalue $\Omega^2(\lambda)$ is a function of the actual growth rate λ. The true eigenmode should be the particular eigensolution of Eq. (28) for which $\Omega^2(\lambda)=0$. Equation (28) constitutes a linear Hermitian eigenvalue problem. The sign of the eigenvalue Ω^2 indicates the stability condition. Actually, $\Omega^2(\lambda)=0$ represents the dispersion relation. The Nyquist diagram can be used to determine the unstable roots. Since the system is Hermitian, the eigenvalues $\Omega^2(\lambda)$ are real, not complex. Therefore, the sign of $\Omega^2(\lambda)$ is sufficient to determine the stability of the system. Only when nonideal MHD effects are taken into account does the problem become non-Hermitian for which a full Nyquist diagram analysis is then required. Note that the growth rate λ actually appears in both the plasma energy and the wall energy. However, as was pointed in Ref. 17 (and also confirmed in numerical computations), the plasma energy does not change significantly with a growth rate that is on the order of the resistive wall mode growth rate for realistic wall conductivities and thicknesses. This implies that only the variation of the wall energy with respect to λ is required to determine the sign of $\Omega(\lambda)$, as long as λ is small enough to neglect the kinetic energy in evaluating the energy of the plasma.

III. NUMERICAL RESULTS

The theoretical formulation of the thick wall described in the preceding section was used to construct a thick-wall numerical code package, which was then incorporated into the AEGIS code. Three benchmarks for this new package were performed. From the energy principle for the wall in Eq. (13), one can see that, if σ is set to vanish, the wall problem becomes vacuumlike. In this case, the three regions corresponding to the inner vacuum, wall, and outer vacuum can be regarded as a single vacuum region extending from the plasma edge to infinity, even though different numerical schemes are used in each of these three regions. The first benchmark study was to compare the code result in the case $\sigma=0$ with that obtained from the GATO code[18] without a conducting wall. The results were found to agree very well. As a further check for the case when $\sigma=0$, the stability properties were numerically confirmed to be independent of the thickness and location of the wall. In another benchmark, we confirmed that the thick-wall result converges to the result calculated from thin-wall theory in the limit as the wall thickness is decreased. For the third benchmark, we used the fact that the growth rate of resistive wall modes has a sharp transition at the critical wall position for perfectly conducting wall stabilization. We were able to observe this transition with the code. Also we did a comparison with analytical theory in the large-aspect-ratio cylindrical case in order to check the diagonal matrix elements. All of these benchmark studies showed a good agreement.

After having performed benchmark studies, we proceeded to use the extended AEGIS code to study the effect of wall thickness on the stability of resistive wall modes for realistic toroidal plasma configurations. In particular, we studied a configuration of the ITER type.[1] The main geometric parameters are as follows: The major radius is 6.2 m, the minor radius is 2.0 m, the elongation of the plasma cross section is 1.86, and the triangularity is 0.5. The safety factor at the 95% flux surface is $q_{95}=3$. One difference with the original ITER design is that the safety factor at the magnetic axis, q_0, was set to have the value 1.05, slightly above unity, which is similar to the so-called "hybrid mode" proposed for ITER. For this configuration with these parameters, the no-wall marginal stability normalized beta limit is $\beta_N=3.4$ and the volume-averaged beta limit is $\langle\beta\rangle=5.5\%$. Because the q_0 value exceeds unity, these β values are higher than those in the Ohmic ITER design (namely, $\beta_N=1.77$ and $\langle\beta\rangle=2.5\%$). We set the value of q_0 to be above unity in order to avoid the excitation of internal kink modes, while allowing the resistive wall modes to arise. The specific equilibrium we inves-

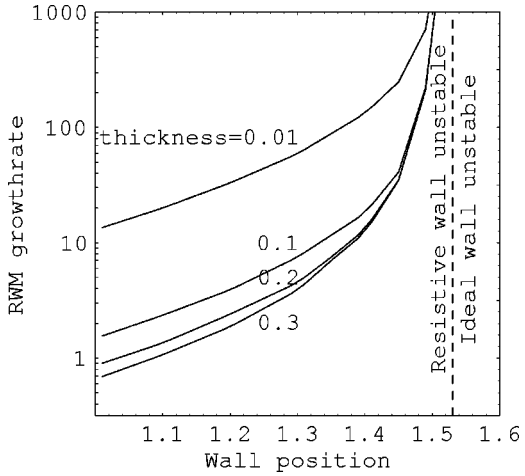

FIG. 1. Resistive wall mode growth rate vs wall position for four different values of the wall thickness.

tigate here for the effect of wall thickness has $\beta_N=3.88$ and $\langle\beta\rangle=6.2\%$, which is above the no-wall limit. The critical position of a perfectly conducting wall for ideal external kink stabilization is $b=1.53$. The equilibrium was generated numerically with the use of the TOQ equilibrium code.[19] The extended AEGIS code reads the TOQ equilibrium data and performs the stability studies. The numerical results are summarized in Figs. 1 and 2.

Figure 1 shows the dependence of the resistive wall mode growth rate on the wall position for four different values of the wall thickness. The growth rate is normalized by the resistive wall diffusion time τ_w for the thickness $d=0.01$. From Fig. 1, one can see that, although the amplitude is different, the growth rate evolves as in the thin-wall case—i.e., the growth rate increases as the wall position increases and becomes very large when the wall position approaches the critical wall position at $b=1.53$. Generally speaking, the growth rate decreases as the wall thickness increases. However, this feature becomes weaker and weaker as the outer wall position moves toward the critical wall position. Near the critical wall position, the growth rate curves corresponding to different values of the wall thickness tend to merge with each other. This is an indication that the portion of the wall outside the critical location does not contribute to reducing the growth rate.

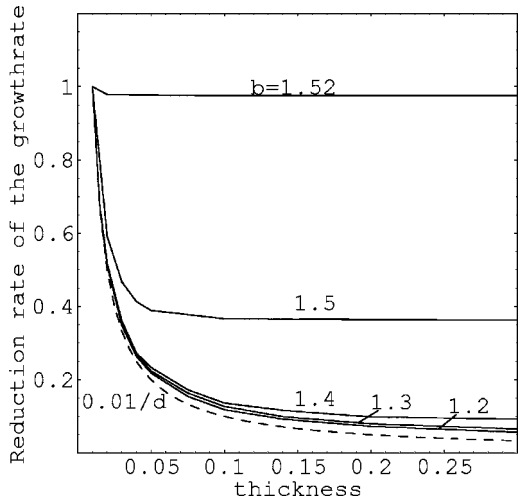

FIG. 2. Change of the resistive wall mode growth rate vs wall thickness, with wall position as the parameter. The dashed curve represents the scaling based on the thin-wall model.

Figure 2 estimates the scaling of the wall thickness effect, with the growth rate normalized to the growth rate for wall thickness 0.01. In the thin-wall theory, the growth rate of the resistive wall mode scales as $1/d$; this thin-wall scaling is represented by the dashed curve in Fig. 2. The numerically computed growth rates are plotted for four different wall positions. The results shown in Fig. 2 indicate that, although the wall thickness effect generally reduces the growth rate of the resistive wall modes, there is a limit in that the portion of the wall located beyond the ideal-wall critical position contributes almost nothing to stabilization. For example, in the $b=1.52$ case, the growth rate stops decreasing as the wall thickness increases to 0.01; in the $b=1.5$ case, it stops decreasing as the wall thickness increases to 0.03, etc. The thin-wall estimate is quite different from the result for the case when the inner side of the wall ψ_{b_1} is close to the critical wall position. The thin-wall estimate is relevant only when the wall is brought very close to the plasma and is not too thick.

IV. CONCLUSIONS AND DISCUSSION

In this paper we have shown how to calculate the effect of finite wall thickness on the stability of resistive wall modes. Beginning from the energy principle, we used the solutions of the Euler-Lagrange equations to minimize the energies in various regions. An equation for the eigenvalue was derived from the matchings at the various interfaces between the plasma and the vacuum regions and between the wall and the vacuum regions. A numerical package developed to handle these interface matchings was added to the AEGIS code in order to provide the capability to investigate the effect of finite wall thickness on resistive wall mode stability. Benchmark studies showed good agreement, especially with the GATO code in the zero-wall-conductivity limit and with the thin-wall model in the limit of decreasing wall thickness. The extended version of the AEGIS code was then used to study the wall thickness effect on resistive wall modes in an ITER-like equilibrium. We found that the realistic thick-wall calculation can be significantly more pessimistic than the conventional thin-wall estimate. The critical wall position for stabilization by a perfectly conducting wall is a key parameter, in the sense that the portion of the wall beyond this critical position provides almost no stabilizing contribution.

The effect of wall thickness on feedback stabilization for the case when the feedback coils are outside the vacuum chamber could also be an important issue. Coupling the current version of the AEGIS code to a code for feedback stabilization is proposed for future investigation. The effect of plasma rotation on resistive mode stability in the presence of a thick wall could also be investigated by a further extension of the AEGIS code; this is now underway.

ACKNOWLEDGMENTS

The authors are indebted to A. Turnbull for his help in the benchmark studies with the GATO code and for many helpful communications. They thank M. S. Chu for helpful discussions. They are also grateful to J. W. Van Dam for his encouragement and advice concerning the AEGIS project.

This research was supported by the Office of Fusion Energy Science of the U.S. Department of Energy under Grant No. DE-FG02-04ER54742.

APPENDIX: THE MATRIX DEFINITIONS IN EQ. (1)

The matrices in Eq. (1) are defined as follows:

$$\mathcal{F} = \mathcal{B} - \mathcal{Q}\mathcal{C}^{-1}\mathcal{Q}^{\dagger},$$

$$\mathcal{K}^{\dagger} = \mathcal{P} - \mathcal{R}\mathcal{C}^{-1}\mathcal{Q}^{\dagger},$$

$$\mathcal{G} = \mathcal{A} - \mathcal{R}\mathcal{C}^{-1}\mathcal{R}^{\dagger},$$

where

$$\begin{pmatrix} \mathcal{A} & \mathcal{P} & \mathcal{R} \\ \mathcal{P}^{\dagger} & \mathcal{B} & \mathcal{Q} \\ \mathcal{R}^{\dagger} & \mathcal{Q}^{\dagger} & \mathcal{C} \end{pmatrix} = \begin{pmatrix} \mathcal{A}_p & \mathcal{P}_p & \mathcal{R}_p \\ \mathcal{P}_p^{\dagger} & \mathcal{B}_p & \mathcal{Q}_p \\ \mathcal{R}_p^{\dagger} & \mathcal{Q}_p^{\dagger} & \mathcal{C}_p \end{pmatrix} + \rho\lambda^2 \begin{pmatrix} \Gamma & \Sigma & \Upsilon \\ \Sigma^{\dagger} & \Xi & \Lambda \\ \Upsilon^{\dagger} & \Lambda^{\dagger} & \Pi \end{pmatrix}.$$

Here ρ is the plasma mass density, and $\boldsymbol{\mathcal{A}}_p$, $\boldsymbol{\mathcal{B}}_p$, etc., are $M \times M$ matrices defined as follows:

$$\mathcal{A}_p = \frac{\chi'^3 q}{g}\mathcal{K}_{\parallel}\langle|\nabla\theta|^2\rangle\mathcal{K}_{\parallel} + \frac{\chi'\chi''^2 q}{g}\langle|\nabla\psi|^2\rangle + \frac{g(q\chi')'^2}{\chi' q}\mathcal{I} + \mu_0 p'\frac{q\chi''}{g}\langle X^2\rangle + \mu_0 P'\frac{\chi' q}{g}\left\langle\frac{\partial X^2}{\partial\psi}\right\rangle - g'q'\chi'\mathcal{I} - i\frac{\chi'^2\chi'' q}{g}(\langle\boldsymbol{\nabla}\psi\cdot\boldsymbol{\nabla}\theta\rangle\mathcal{M} - \mathcal{M}\langle\boldsymbol{\nabla}\psi\cdot\boldsymbol{\nabla}\theta\rangle),$$

$$\mathcal{B}_p = \frac{\chi' g}{n^2 q}\mathcal{K}_{\parallel}\mathcal{K}_{\parallel},$$

$$\mathcal{C}_p = \frac{\chi' g}{q}\mathcal{M}\mathcal{M} + \frac{n^2\chi'^3 q}{g}\langle|\nabla\psi|^2\rangle,$$

$$\mathcal{P}_p = 0,$$

$$\mathcal{Q}_p = \frac{\chi' g}{nq}\mathcal{M}\mathcal{K}_{\parallel},$$

$$\mathcal{R}_p = i\frac{n\chi'^3 q}{g}\langle\boldsymbol{\nabla}\psi\cdot\boldsymbol{\nabla}\theta\rangle\mathcal{K}_{\parallel} - \mu_0 nP'\frac{\chi' q}{g}\langle X^2\rangle - \frac{n\chi'^2\chi'' q}{g}\langle|\nabla\psi|^2\rangle - n\chi' q g'\mathcal{I},$$

$$\Gamma = \frac{\chi'^3 q}{g}\left(\left\langle\frac{1}{B^2}\right\rangle + q^2\left\langle\frac{X^2|\boldsymbol{\nabla}\theta|^2}{B^2}\right\rangle\right),$$

$$\Xi = \frac{\chi'^3 q}{n^2 g}\left\langle\frac{X^2|\nabla\psi|^2}{B^2}\right\rangle,$$

$$\Pi = n^2\Xi,$$

$$\Sigma = -i\frac{\chi'^3 q^2}{ng}\left\langle\frac{X^2\boldsymbol{\nabla}\psi\cdot\boldsymbol{\nabla}\theta}{B^2}\right\rangle,$$

$$\Lambda = n\Xi,$$

$$\Upsilon = n\Sigma.$$

The angle bracket $\langle\cdots\rangle$ represents the associated Fourier matrix, whose elements are defined as follows:

$$\langle\cdots\rangle_{mm'} = \frac{1}{2\pi}\int_{-\pi}^{\pi} d\theta(\cdots)\exp\{i(m'-m)\theta\},$$

and $\mathcal{K}_{\parallel mm'} = (m-nq)\mathcal{I}_{mm'}$, $\mathcal{M}_{mm'} = m\mathcal{I}_{mm'}$, and $\mathcal{I}_{mm'} = 1$ for $m = m'$, otherwise, $\mathcal{I}_{mm'} = 0$, where $m, m' = 1, 2, \ldots, M$. Here, X is the distance from the axisymmetric axis, and the poloidal and the toroidal fluxes χ and g are defined by $\mathbf{B} = \chi'\boldsymbol{\nabla}\phi \times \boldsymbol{\nabla}\psi + g\boldsymbol{\nabla}\phi$.

[1] R. Aymar, P. Barabaschi, and Y. Shimomura, Plasma Phys. Controlled Fusion **44**, 519 (2002).
[2] F. Troyon, R. Gruber, H. Saurenmann, S. Semenzato, and S. Succi, Plasma Phys. Controlled Fusion **26**, 209 (1984).
[3] A. D. Turnbull, A. Roy, O. Sauter, and F. S. Troyon, Nucl. Fusion **28**, 1379 (1988).
[4] A. D. Turnbull, F. Yesseen, A. Roy, O. Sauter, and W. A. Copper, Nucl. Fusion **29**, 629 (1989).
[5] G. Schultz, A. Bondeson, F. Troyon, and A. Roy, Nucl. Fusion **30**, 2259 (1990).
[6] A. D. Turnbull, Y. R. Lin-Liu, R. L. Miller, T. S. Taylor, and T. N. Todd, Phys. Plasmas **6**, 1113 (1999).
[7] J. P. Freidberg, *Ideal Magnetohydrodynamics* (Clarendon, Oxford, 1987).
[8] A. Bondeson and D. J. Ward, Phys. Rev. Lett. **72**, 2709 (1994).
[9] R. Betti and J. P. Freidberg, Phys. Rev. Lett. **74**, 2949 (1995).
[10] R. Fitzpatrick and A. Aydemir, Nucl. Fusion **36**, 11 (1996).
[11] B. Hu and R. Betti, Phys. Rev. Lett. **93**, 105002 (2004).
[12] L.-J. Zheng, M. Kotschenreuther, and M. S. Chu, "Rotation stabilization of the resistive wall modes due to the shear Alfvén resonance," Phys. Rev. Lett. (submitted).
[13] E. J. Strait, Phys. Plasmas **1**, 1415 (1994).
[14] M. S. Chu, V. S. Chan, M. S. Chance, D. H. Edgell, A. M. Garofalo, A. H. Glasser, S. C. Guo, D. A. Humphreys, T. H. Jensen, J. S. Kim, R. J. La Haye, L. Lao, G. A. Navratil, M. Okabayashi, F. W. Perkins, H. Reimerdes, H. E. St. John, E. Soon, E. J. Strait, A. D. Turnbull, M. L. Walker, and S. K. Wong, Nucl. Fusion **43**, 196 (2003).
[15] L.-J. Zheng and M. Kotschenreuther, "AEGIS: An adaptive ideal magnetohydrodynamics shooting code for axisymmetric plasmas," J. Comput. Phys. (submitted).
[16] M. S. Chance, Phys. Plasmas **4**, 2161 (1997).
[17] S. W. Haney and J. P. Freidberg, Phys. Fluids B **1**, 1637 (1989).
[18] L. C. Bernard, F. J. Helton, and R. W. Moore, Comput. Phys. Commun. **24**, 377 (1981).
[19] R. L. Miller and J. W. Van Dam, Nucl. Fusion **27**, 2101 (1987).